$B(E2)$ measurements in the yrast band of ^{28}Mg: Implications for the $N = 20$ island of inversion

M. S. Martin,[1,*] H. Asch,[1] G. C. Ball,[2] P. E. Garrett,[3] A. B. Garnsworthy,[2] C. J. Griffin,[2] G. Hackman,[2] G. Hagen,[4,5,2] K. D. Launey,[6] G. Leckenby,[2,7] J. Liang,[2,8] R. S. Lubna,[2,†] C. R. Natzke,[2,9] C. Pearson,[2] A. Redey,[10] G. H. Sargsyan,[11] P. C. Srivastava,[12] K. Starosta,[13,‡] Z. H. Sun,[4] C. E. Svensson,[3] S. Upadhyayula,[2,§] K. van Wieren,[14] V. Vedia,[2] J. Williams,[2] A. Woinoski,[1] F. Wu (吴桐安),[13] D. Yates,[2,7] and Z. Yu[13]

[1]*Department of Physics, Simon Fraser University, Burnaby, British Columbia, Canada, V5A 1S6*
[2]*TRIUMF, Vancouver, British Columbia, Canada, V6T 2A3*
[3]*Department of Physics, University of Guelph, Guelph, Ontario, Canada, N1G 2W1*
[4]*Physics Division, Oak Ridge National Laboratory, Oak Ridge, Tennessee 37831, USA*
[5]*Department of Physics and Astronomy, University of Tennessee, Knoxville, Tennessee 37996, USA*
[6]*Department of Physics and Astronomy, Louisiana State University, Baton Rouge, Louisiana 70803, USA*
[7]*Department of Physics and Astronomy, University of British Columbia, Vancouver, British Columbia, Canada, V6T 1Z1*
[8]*Department of Physics and Astronomy, Saint Mary's University, Halifax, Nova Scotia, Canada, B3H 3C3*
[9]*Department of Physics, Colorado School of Mines, Golden, Colorado 80401, USA*
[10]*School of Engineering Science, Simon Fraser University, Burnaby, British Columbia, Canada, V5A 1S6*
[11]*Facility for Rare Isotope Beams, Michigan State University, East Lansing, Michigan 48824, USA*
[12]*Department of Physics, Indian Institute of Technology Roorkee, Roorkee, Uttarakhand 247667 India*
[13]*Department of Chemistry, Simon Fraser University, Burnaby, British Columbia, Canada, V5A 1S6*
[14]*Science Technical Centre, Simon Fraser University, Burnaby, British Columbia, Canada, V5A 1S6*

(Received 18 August 2023; revised 12 July 2024; accepted 19 August 2024; published 13 September 2024)

High-precision lifetime measurements in ^{28}Mg were performed to study neutron shell evolution in Mg isotopes and the onset of the $N = 20$ island of inversion. Using both the recoil distance and Doppler shift attenuation methods, five lifetimes were measured in addition to six upper limits. The observation of two long-lived, negative-parity states demonstrate the importance of studying Mg isotopes for the contribution of intruder configurations to *sd*-shell nuclei. Lifetimes of the 2_1^+ and 4_1^+ states of 1.81(5) ps and $172(^{+11}_{-10})_{\text{stat.}}(4)_{\text{stop.}}(8)_{\text{feed.}}(4)_{\text{targ.}}$ fs, respectively, demonstrate a loss of collectivity with increasing spin in the yrast band, permitting for distinguishing between current theoretical models. These measurements also highlight the progression of yrast structure across the Mg isotopic chain from rotational at $N = 12$ to large shape mixing at $N = 16$ and back to collective behavior at $N = 20$ but with dominating intruder configurations.

DOI: 10.1103/PhysRevC.110.034314

I. INTRODUCTION

In 1975, Tibault *et al.* noted that experimental data in Na isotopes near $N = 20$ were inconsistent with a "classical shell closure" effect and were more closely described as a "region of sudden deformation" [1]. It is now understood that this region is one where isospin dependent components of the nuclear interaction, such as the noncentral tensor components, substantially contribute to nuclear observables, and the nominal shell gaps predicted by the spherical shell-model change (e.g., Refs. [2–6]). In a number of nuclei in this *island of inversion*, centered around ^{32}Mg, the 2p2h and 4p4h configurations across the nominal $N = 20$ shell gap are energetically favored in the ground state over the 0p0h configurations (e.g., Refs. [7,8] for ^{32}Mg and Ref. [9] for ^{31,33}Mg). In nuclei closer to stability, enhanced contributions from particle-hole excitations across the $N = 20$ shell gap can be seen in excited states (e.g., Refs. [10,11]). This region of the nuclear chart has been of significant interest to nuclear structure research for decades (e.g., Refs. [12–16]) and continues to remain active, with many studies being performed in the past few years (e.g., Refs. [17–23]).

Band structures in nuclei are typically studied using relative excitation energies or transition strengths between states (e.g., Refs. [24,25]). As excitation energies can be reproduced using a variety of theoretical wave functions given appropriate model Hamiltonians, transition strengths provide the advantage of electromagnetic transition operators being well defined and thus being a more direct probe of the nuclear wave function. Single-particle structures, where nucleons act

*Contact author: matthew.martin@anl.gov; Present address: Physics Division, Argonne National Laboratory, Lemont, Illinois 60439, USA.

†Present address: Facility for Rare Isotope Beams, Michigan State University, East Lansing, Michigan 48824, USA.

‡Contact author: starosta@sfu.ca

§Present address: Lawrence Livermore National Laboratory, Livermore, California 94550, USA.

independently, result in small $B(E2)$ values which decrease with increasing spin, while collective behavior is generally seen through increasing $B(E2)$ transition strengths with increasing spin, scaling as the square of Clebsch-Gordan coefficients for collective rotation or linearly with the number of phonons for effective collective vibrations [26].

Studies of the Mg isotopic chain allow examination of neutron shell structure from the neutron deficient shell closure at $N = 8$ (^{20}Mg) to beyond the nominal shell closure at $N = 20$ (^{32}Mg), located at the *heart* of the island of inversion. Though specific measurements of Mg isotopes which encompass the entire range of the neutron *sd* shell have recently been made (e.g., Refs. [27–35]), these include few high-precision transition rate measurements on the neutron-rich side of the valley of stability. Additional precision measurements will provide clarity on the structure of these nuclei as well as the evolution of neutron shells between stability and the $N = 20$ island of inversion.

Theoretical calculations of nuclear properties face two main problems: the underlying interactions which govern the behavior of nucleons and solving the many-body problem. In *sd*-shell nuclei, the latter can be handled in a variety of different ways, and thus these nuclei become testing grounds for studying the underlying nuclear interactions. With $N = 16$, ^{28}Mg lies halfway between the stable, $N = Z$, ^{24}Mg, and the $N = 20$ island of inversion nucleus, ^{32}Mg, making studies of ^{28}Mg essential for understanding how neutron shells evolve with increasing occupation in the *sd* shell. Both phenomenological and *ab initio* methods are able to reproduce energies of low-lying excited states in ^{28}Mg with reasonable accuracy (e.g., see Figs. 10 and 11 in Ref. [33]); however, calculations of transition strengths within the yrast band vary wildly. Previous experimental results by Fintz *et al.* [36,37] and Fisher *et al.* [38] had disagreeing results for the $4^+_1 \to 2^+_1$ transition strength and large uncertainties in the $2^+_1 \to 0^+_{\mathrm{g.s.}}$ transition strength, preventing any firm conclusions on the degree of collectivity in the yrast band of ^{28}Mg from being made. Recently, Williams *et al.* performed Doppler shift attenuation method (DSAM) lifetime measurements in ^{28}Mg and were able to precisely measure the transition strength of the $4^+_1 \to 2^+_1$, with results agreeing with Fisher *et al.* and indicating weak collectivity in the yrast band [33]. The DSAM measurement was insensitive to the $2^+_1 \to 0^+_{\mathrm{g.s.}}$ lifetime, continuing to prevent any firm conclusions from being made. In this work, we present results from complementary lifetime measurements in ^{28}Mg. These results include negative-parity states, allowing to investigate the impact of intruder *pf*-shell orbitals on the structure of ^{28}Mg, and positive-parity states, which highlight the structural evolution across the Mg isotopic chain from stability to the $N = 20$ island of inversion.

II. EXPERIMENTAL DETAILS

In the presented experiment, ^{28}Mg was populated through the fusion-evaporation reaction $^{12}\mathrm{C}(^{18}\mathrm{O}, 2p)^{28}\mathrm{Mg}$ using a beam of ^{18}O at 3.22 MeV/u delivered by the ISAC-II [39] facility at TRIUMF, Canada's particle accelerator center. Isolation of the weak $2p$ reaction channel was made possible through the combination of the 16 clover-type HPGe detectors of the TIGRESS array [40] for γ-ray detection and the 128-element CsI(Tl) ball [41], part of the suite of ancillary detectors developed for the TIGRESS Integrated Plunger (TIP) [42], for charged particle detection.

This experiment was performed in two parts to provide sensitivity to lifetimes at different scales. To measure longer ($\gtrsim$1 ps) lifetimes, the recoil distance method (RDM) outlined in Ref. [43] was used with a target-stopper combination. The target consisted of 460 μg/cm^2 ^{12}C deposited by MICROMATTER [44] onto an 8.87-mg/cm^2 ^{197}Au foil. The stopper used was 12.8 mg/cm^2 $^{\mathrm{nat.}}$Ag. The plunger device developed for TIP, discussed in Refs. [42,45], was employed with the Au and Ag layers forming a parallel plate capacitor, allowing us to measure and maintain consistent target-stopper separations as outlined in Ref. [46]. Eleven total target-stopper separation distances ranging from ≈ 17 μm to ≈ 400 μm were used to reduce systematic errors of the measurement. The calibration of the absolute separation of the target and stopper was measured to ±5 μm precision using the methods described in Ref. [46]. To measure shorter ($\lesssim$ 1 ps) lifetimes, the DSAM outlined in Ref. [47] was used. The DSAM target consisted of a 394-μg/cm^2 ^{12}C foil adhered to a 24-mg/cm^2 $^{\mathrm{nat.}}$Pb backing, with a 200-μg/cm^2 In layer between the two used for adhesion [48]. A 8.87-mg/cm^2 ^{197}Au foil was adhered to the upstream side of the carbon target to replicate the conditions of the RDM experiment.

Data were collected using the newly implemented triggerless data acquisition system (DAQ) described in Ref. [49]. The online filter was set to collect events consisting of at least two charged particle detections in the CsI(Tl) ball and at least one γ ray in the TIGRESS HPGe crystals within a 2.5-μs coincidence window. Offline separation was performed using time-coincidence windows of 130 ns (TIGRESS-TIGRESS), 200 ns (CsI-CsI), and 300 ns (TIGRESS-CsI) to reduce the number of random events in the data set. Particle identification methods, described in Ref. [41], were used to isolate 2p events which produce ^{28}Mg from other observed reaction channels. The cross section for production of ^{28}Mg is estimated at ≈0.2 mb assuming an average beam current of 2.5×10^9 particles per second and 75% population of the 2^+_1 state. Data were collected over ≈ 1 week, with $\approx 6 \times 10^6$ 2p events collected using the DSAM target and $\approx 1 \times 10^6$ 2p events collected for each RDM distance.

III. SPECTROSCOPY

The RDM data at all 11 target-stopper distances were summed and Doppler corrected to determine γ-ray energies and intensities and develop a level scheme. Spectra derived from summed and Doppler-corrected RDM data gated on the $4^+_1 \to 2^+_1$ and $2^+_1 \to 0^+_{\mathrm{g.s.}}$ transitions, used to construct the level scheme, are shown in the top and bottom of Fig. 1, respectively.

Of particular interest here was a state at $E \approx 6140$ keV first observed in Ref. [50], prompted by the observation reported in Ref. [33] that this state is long lived. In this work, the Doppler-corrected and summed RDM data showed no clear

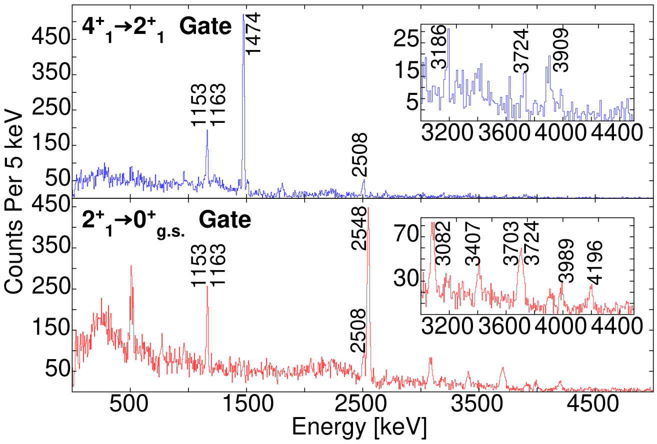

FIG. 1. Background subtracted, Doppler-corrected γ-ray energy spectra using summed RDM data from all 11 target-stopper distances. Gamma rays shown are in coincidence with the $4^+_1 \to 2^+_1$ (top) and $2^+_1 \to 0^+_{g.s.}$ (bottom) transitions. The two shoulder peaks surrounding the $E \approx 1474$ keV $2^+_1 \to 0^+_{g.s.}$ transition in the $4^+_1 \to 2^+_1$ gated spectrum indicates that stopped components are present. Inserts show regions from 3000 to 4500 keV binned in 10 keV per bin (top) and 5 keV per bin (bottom).

indication that a transition was present at this energy; however, a stopped transition at 4667(2) keV was observed in the DSAM data in coincidence with the $2^+_1 \to 0^+_{g.s.}$ transition; see Fig. 2. With this observation, and the previous data suggesting the corresponding 6141(2)-keV state is long lived, the DSAM data were used to determine the γ-ray energy and intensity of this transition.

In total, 14 transitions originating from 13 independent levels were observed, all of which were previously identified in Ref. [33]. Only the long-lived state, at an excitation energy of 6141(2) keV, deduced from the observation of the 4667(2)-keV γ ray, was placed using the DSAM data. The remaining states were placed using the Doppler-corrected and summed RDM data. The complete level scheme developed in this work is shown in Fig. 3.

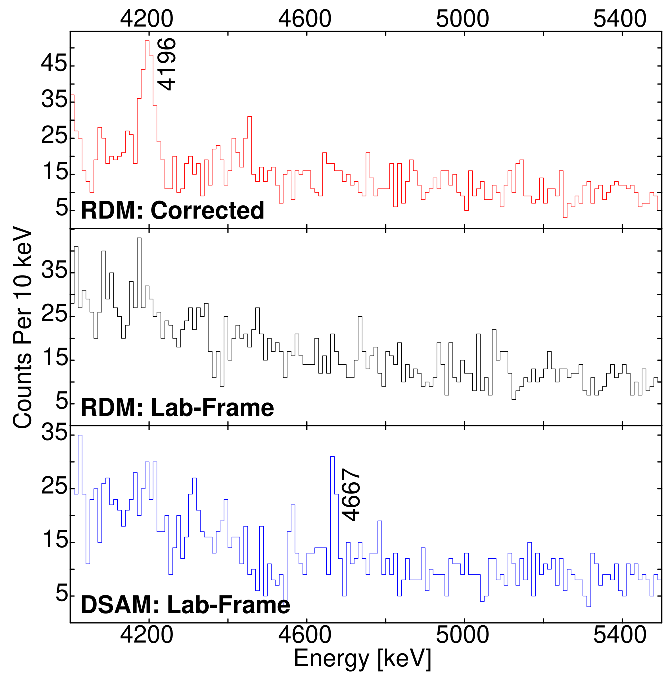

FIG. 2. Gamma-ray energy spectra, gated on the $2^+_1 \to 0^+_{g.s.}$ transition, showing the observation of a peak at 4667(2) keV. Spectra shown for the Doppler-corrected and summed RDM data (top), laboratory-frame or uncorrected RDM data (middle), and laboratory-frame DSAM data (bottom). The spectra confirm the existence of a long-lived state in ^{28}Mg which decays by emission of the 4667(2) keV γ ray. See text for further discussion.

IV. LIFETIME MEASUREMENTS

Excited state lifetimes were determined using RDM and DSAM following the procedure of Ref. [51], where simulated spectra at various lifetimes are compared to experimental data. Best-fit parameters were extracted by minimizing the χ^2 using the likelihood-ratio χ^2 method described in Ref. [52]. A summary of observed γ rays, corresponding excited states, and measured lifetimes is shown in Table I.

TABLE I. Summary of results for states observed in ^{28}Mg. Spin-parity assignments from Refs. [33,55]. All other measurements are from this work. Uncertainties are reported at 1σ, while limits are reported at 90% confidence.

J^π	E_{level} (keV)	E_γ (keV)	I_γ	τ (fs)
2^+	1473.8(6)	1473.8(6)	1.000(16)	$1.81(5) \times 10^3$
4^+	4021.8(9)	2547.8(7)	0.235(8)	$1.72(^{+0.11}_{-0.10})_{\text{stat.}}(4)_{\text{stop.}}(8)_{\text{feed.}}(4)_{\text{targ.}} \times 10^2$
2^+	4556.4(14)	3082.4(13)	0.041(4)	< 24
2^+	4881(2)	3407(2)	0.017(3)	< 24
3^-	5174.5(14)	1152.7(10), 3703(3)	0.023(7), 0.038(5)	$1.2(3)_{\text{stat.}}(1)_{\text{stop.}}(1)_{\text{targ.}} \times 10^2$
(4^+)	5184.0(11)	1162.2(6)	0.061(8)	< 37
2	5463(2)	3989(2)	0.012(2)	
2^+	5670(3)	4196(3)	0.010(3)	< 71
$(0, 4)^-$	6141(2)	4667(2)	0.006(2)	$1.0(^{+0.8}_{-0.2}) \times 10^3$
$(4, 5)^-$	6530.3(14)	2508.4(11)	0.031(4)	$3.9(^{+0.8}_{-0.7})_{\text{stat.}}(5)_{\text{stop.}}(2)_{\text{targ.}} \times 10^2$
$(2^+, 3, 4^+)$	7208(3)	3186(3)	0.009(3)	
(5)	7746(3)	3724(3)	0.009(3)	< 49
(6^+)	7931(3)	3909(3)	0.011(2)	< 41

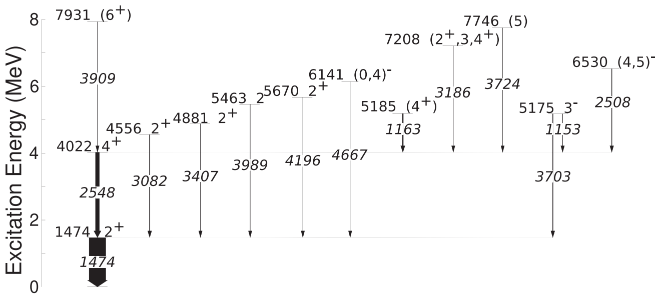

FIG. 3. Level scheme of ^{28}Mg observed using Doppler-corrected and summed RDM data, along with stopped DSAM data. Spin-parity assignments are from Ref. [33]. Width of connecting arrows indicates observed intensities of γ rays.

Simulations used in this work were previously developed under the GEANT4 Monte Carlo framework for experiments employing the combination of TIP and TIGRESS (e.g., Ref. [53]). Modifications to the fusion-evaporation mechanism were made such that protons were evaporated according to Weisskopf's statistical evaporation model [54], with an effective Coulomb barrier and equilibrium temperature of the compound nucleus fit to charged particle energy spectra taken with the CsI(Tl) ball. On fitting charged particle evaporation parameters, observed Doppler shifts in the simulated TIGRESS γ-ray spectra were found to agree with experimental data without further changes. Based on GEANT4 simulations, residual ^{28}Mg nuclei were expelled from the back of the ^{12}C target with a centroid speed of $\beta \approx 0.037$ with a standard deviation of 0.004.

Gamma-ray data were grouped into TIGRESS rings, giving six unique polar angles for which measurements and simulations could be compared: Two each downstream (rings 1 and 2, $\theta \approx 45^\circ$), the corona (rings 3 and 4, $\theta \approx 90^\circ$), and upstream (rings 5 and 6, $\theta \approx 135^\circ$). For states with observed feeding transitions, lifetimes of higher-lying states were determined and incorporated into GEANT4 simulations of cascading decays for lower-lying states.

A. Effective lifetimes

Of the 13 unique levels identified in this work, only the 4_1^+ and 2_1^+ states were observed to be fed by higher-lying states, and the feeding correction procedure is discussed below. For the remaining 11 states, lifetimes determined are considered *effective* lifetimes as absolute lifetimes may be affected by unobserved feeding which was nonetheless present.

The (6_1^+) yrast state, along with five other states, had effective lifetimes sufficiently short that no minimum in the χ^2 curve existed. Instead, the χ^2 continued decreasing for simulated lifetimes approaching and including $\tau = 0$, see Fig. 4(a), indicative of the lifetime of the state being shorter than the sensitive range of DSAM. Lifetime limits were placed at the 90% confidence level using either a second- or third-degree polynomial fit to the curve, using whichever of the two resulted in a more conservative limit. For the (6_1^+) state, the limit was placed at 41 fs and is nearly identical to the 42-fs upper limit placed by Williams *et al.* in Ref. [33].

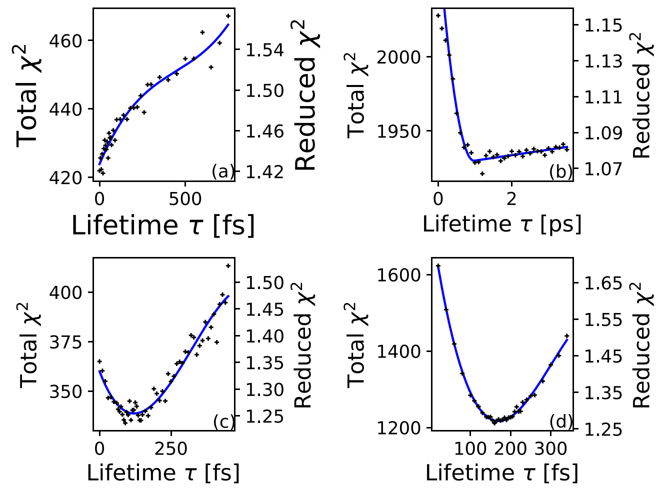

FIG. 4. Curves showing χ^2 as a function of simulated lifetime for the (a) 7931(3)-keV (6_1^+) yrast state, (b) 6141(2)-keV long-lived negative-parity state, (c) 5174.4(14) keV state, and (d) 4021.8(9)-keV 4_1^+ yrast state. Black points are χ^2 values for individual simulations, all using ICRU stopping power tables. Blue curves are third-order polynomial fits to data points for (a), (c), and (d), while a piecewise fit using a second- and first-order polynomial was used in (b). See text for further discussion.

The lifetime of the 6141(2)-keV state was determined to be $1.0(^{+0.8}_{-0.2})$ ps in an analogous manner using DSAM data. The χ^2 was found to decrease with increasing lifetime before the curve flattened and started to increase linearly. The fit shown in Fig. 4(b) to the data is a piecewise fit using both a second- and first-order polynomial under conditions that the two functions are both continuous and smooth at the intersection point, which was left as a free parameter in the fit. Statistics in the individual RDM datasets for each distance were too limited for a measurement to be made. The lower bound of the measurement made here is lower than the 90% confidence limit placed in Ref. [33] but confirms that the state is relatively long lived.

Two precision effective lifetimes were also made using DSAM, where minima in the χ^2 curves were observed. The states for which these measurements were made were the 5174.5(14) keV [shown in Fig. 4(c)] and 6530.3(14)-keV states. Statistical uncertainties (stat.) were taken at $\chi^2_{\mathrm{min.}} + 1$ and scaled by $(\chi^2_{\nu,\mathrm{min.}})^{1/2}$ to account for deficiencies in the model as suggested by the Particle Data Group [56]. For effective lifetimes, uncertainties were estimated for stopping powers of materials and target thicknesses. Stopping power uncertainties (stop.) were estimated by employing both ICRU [57] and SRIM [58] stopping power tables into the GEANT4 simulations and determining best-fit lifetimes using both. The effective lifetimes were then taken as the average value of the two weighted by statistical uncertainties, with the full difference taken as the 1σ uncertainty estimate (see Fig. 1 and accompanying text of Ref. [59]). Target thickness uncertainties (targ.) were estimated by adjusting the target foil thicknesses by $\pm 10\%$ in the GEANT4 simulations, and using the full difference as the 1σ estimate.

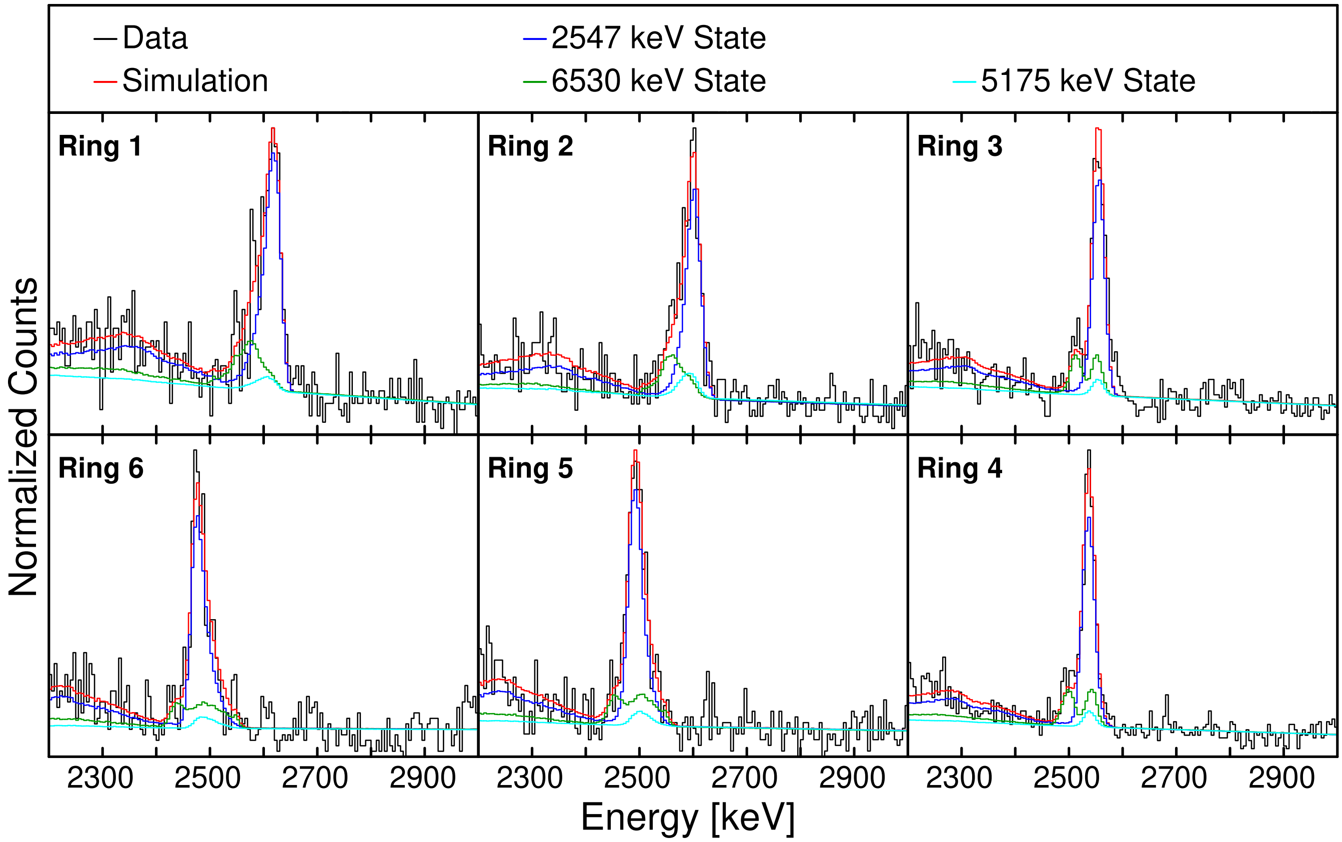

FIG. 5. Simulated lineshapes for the $4_1^+ \rightarrow 2_1^+$ transition at the best fit lifetime of 172 fs. Experimenal spectra (black) compared against the full simulated spectra (red) for all six rings of TIGRESS. The full simulated spectra are linear combinations of direct population of the 4_1^+ state (blue), feeding from the 6530-keV state (green) and feeding from the 5175-keV state (cyan). Simulations shown are performed using ICRU stopping power tables.

B. Lifetime of the 4_1^+ state

The 4_1^+ state was found to be fed by many transitions including two with effective lifetimes long enough to be measured using DSAM. The lineshape of a feeding transition from a state placed at 6530.3(14) keV [$E_\gamma = 2508.4(11)$ keV] was found to be overlapping with the lineshape of the $4_1^+ \rightarrow 2_1^+$ transition, so the two lifetimes were fit simultaneously. While correlation between the two lifetimes is present, with a longer feeder lifetime corresponding to a shorter lifetime of the 4_1^+ state as expected, the correlation is minimal when compared to the statistical uncertainty. This allowed the statistical uncertainty to be determined using a one-dimensional (1D) χ^2 curve shown in Fig. 4(d) and a systematic uncertainty for the lifetime of the feeder states (feed.) to be estimated separately. Specifically, this systematic uncertainty was estimated by adjusting all feeder lifetimes by $\pm 1\sigma$ and taking the difference in the resulting best-fit lifetime of the 4_1^+ state as the 1σ estimate. The lifetime of the 4_1^+ state was determined to be $172(^{+11}_{-10})_{\text{stat.}}(4)_{\text{stop.}}(8)_{\text{feed.}}(4)_{\text{targ.}}$ fs. A comparison between simulated spectra at the best fit lifetime and experimental data is shown in Fig. 5.

The measured lifetime of the 4_1^+ state agrees with the previous measurement by Williams *et al.* in Ref. [33], though with a significant reduction in uncertainty. This reduction is, at least in part, due to the difference in stopping powers between the Pb backing used in this work compared to the Au backing used in Ref. [33]. As the stopping power of ^{28}Mg in Pb is known to be less than that in Au, the stopping time in Pb is longer and thus the time at which the simulated speed of the residual nuclei diverge between stopping power models occurs later during the stopping history. Importantly, with the use of a different backing material, the measurement presented here is complementary to that of Ref. [33] and there is good agreement between the two.

C. Lifetime of the 2_1^+ state

In this work, the 2_1^+ state was found to be predominantly populated directly by the fusion-evaporation reaction or via unobserved feeding, with the most prominent observed feeding transition originating from the 4_1^+ state. While no transitions in ^{28}Mg were seen overlapping with the $2_1^+ \rightarrow 0^+_{\text{g.s.}}$ γ ray, stopped transitions at 1439 and 1525 keV obstructed the lineshape. Analysis of these two transitions revealed that they were from ^{31}Si and ^{42}Ca respectively, nuclei not accessible to the ^{30}Si compound nucleus produced. Additional transitions observed, both within the 2p gate and other charged particle gates, led to the conclusion that both ^{16}O and ^{28}Si were building on the target apparatus throughout the experiment. The presence of ^{31}Si and ^{42}Ca were the result of ^{16}O(^{18}O, $2pn$) and ^{28}Si(^{18}O, $2p2n$) fusion-evaporation

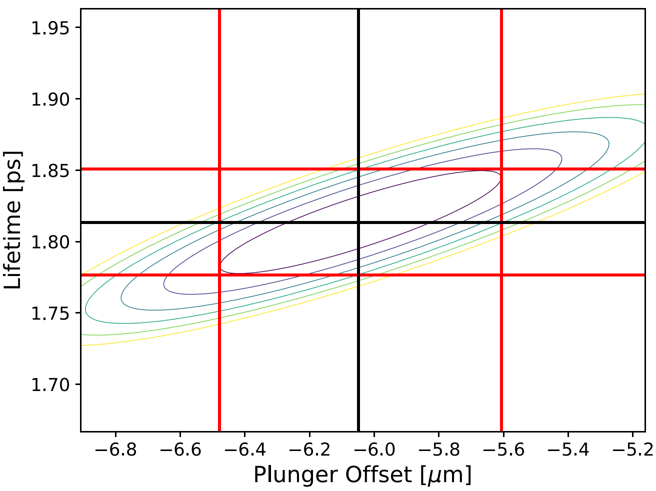

FIG. 6. Analytical form of the χ^2 surface for simultaneous fit of the 2_1^+ state lifetime and the plunger offset parameter d. The minimum of this curve is at $\tau = 1.81(4)$ and $d = -6.0(4)$. Contours display integer number of standard deviations from the minimum before inflation of statistical uncertainties.

reactions respectively. Consequently, charged particle gating did not provide means for removing contaminating γ-ray transitions from RDM spectra of interest. Gating on the $4_1^+ \rightarrow 2_1^+$ transition in ^{28}Mg did remove both these contaminant transitions from the γ-ray spectra but reduced statistics such that the stopped component of the $2_1^+ \rightarrow 0_{\text{g.s.}}^+$ lineshape became indistinguishable from background at close target-stopper distances.

To address the presence of contaminants, spectra simulated for the analysis of the $2_1^+ \rightarrow 0_{\text{g.s.}}^+$ decay included a linear combination of three simulations: simulation of the transition with direct population of the 2_1^+ state, simulation of the $4_1^+ \rightarrow 2_1^+ \rightarrow 0_{\text{g.s.}}^+$ cascade, and simulations of the spectra for the contaminants. The contributions from contaminants were determined independently for each distance as the contaminants grew during the experiment. Coefficients of the linear combination were allowed to vary within the 1σ uncertainty bounds of measured intensities to offset any angular distribution, spin deorientation, or other effects.

As the uncertainty on the absolute target-stopper separation distance was 5 μm, an offset in this separation was included in simulations as a free parameter and simultaneously fit alongside the lifetime of the 2_1^+ state. All 11 target-stopper distances were simulated and compared against experimental data, with the total χ^2 being a sum of the χ^2 values from all six TIGRESS rings from all 11 distances. The analytical fit to the 2D χ^2 surface produced is shown in Fig. 6, and

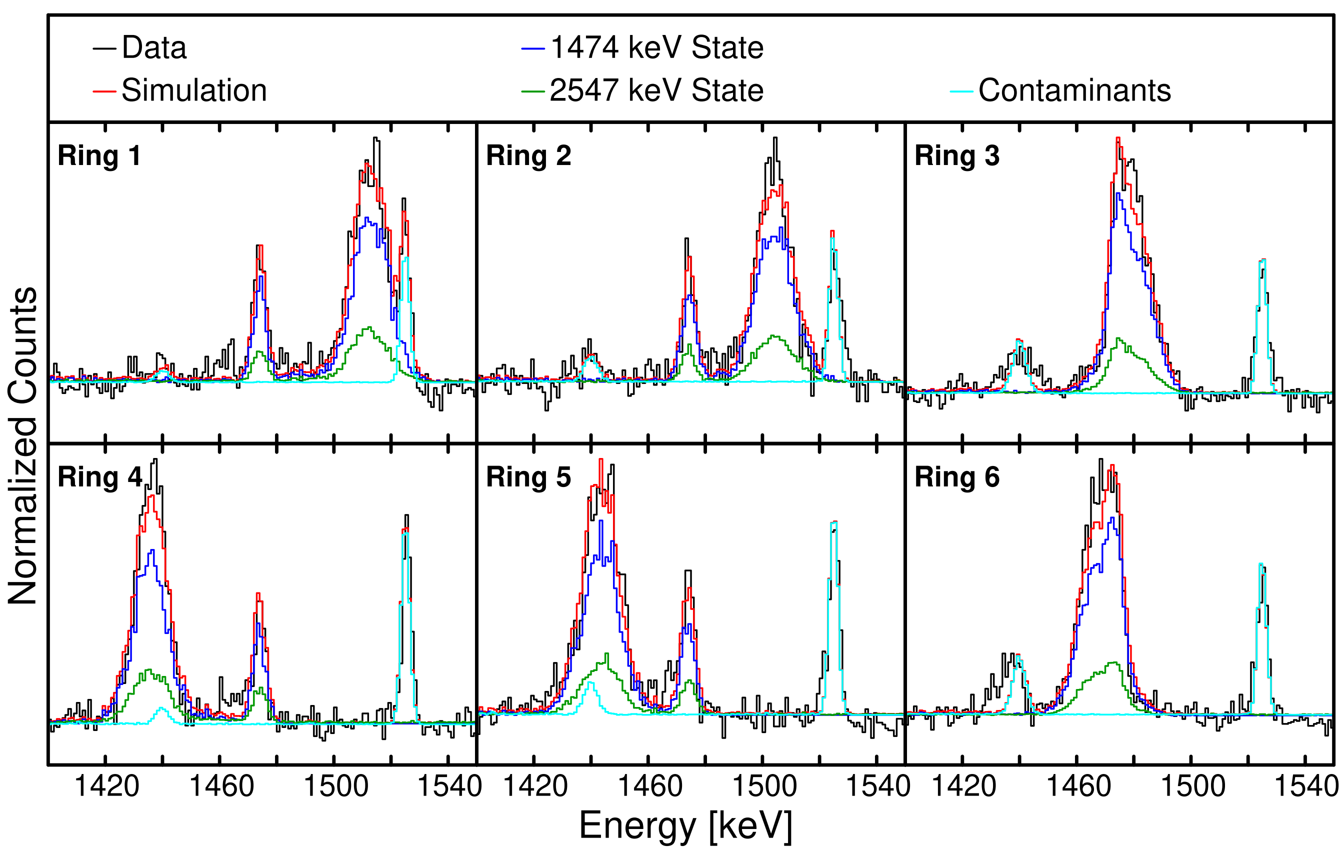

FIG. 7. Simulated lineshapes for the $2_1^+ \rightarrow 0_{\text{g.s.}}^+$ transition at the best fit lifetime of 1.81 ps and separation of $d = 27.9$ μm ($d = 33.9$ μm-6.0 μm $= 27.9$ μm). Experimenal spectra (black) compared against the full simulated spectra (red) for all six rings of TIGRESS. The full simulated spectra are linear combinations of direct population of the 2_1^+ state (blue), feeding from the 2547 keV state (green), and contaminant transitions (cyan).

has contours representing integer number of standard deviations from the minimum. Black and red lines indicate the minimum and 1σ standard deviations in the two parameters, before the statistical uncertainty was inflated by $(\chi^2_{\nu,\mathrm{min.}})^{1/2}$. The best fit lifetime of the 2_1^+ state was determined to be 1.81(5) ps with an offset in the absolute target-stopper separation of $-6.0(6)$ µm. Figure 7 shows the simulated spectra at the best fit lifetime for for the target-stopper distance $d = 27.9$ µm ($d = 33.9$ µm-6.0 µm $= 27.9$ µm) compared to experimental data.

In addition to the measurement described above, the lifetime of the 2_1^+ state was determined using data gated on the $4_1^+ \rightarrow 2_1^+$ transition to ensure that feeding was properly accounted for. Though statistics were severely limited using these gated data, a lower lifetime limit of 1.6 ps was able to be placed using DSAM, and a measurement of $\tau = 1.8(2)$ ps with an offset of $d = -5(^{+3}_{-2})$ µm was made using RDM data; both of these measurements are consistent with the minimum shown in Fig. 6.

The measured lifetime of the 2_1^+ state is consistent with all three previous measurements [33,36,38], however with a greatly reduced uncertainty. It is also consistent with the adopted lifetime of 1.73(14) ps from Ref. [55], a weighted average of the measurements of Refs. [36,38], with a reduction in uncertainty of a factor of ≈ 3. The reduction in uncertainty here is attributed to the RDM technique used, as all three previous measurements were performed using DSAM techniques, which as confirmed in this work is sensitive to shorter-lived states.

V. SCIENTIFIC IMPACT AND DISCUSSION

A. Long-lived negative-parity states

In this work, two long-lived states were observed, both of which were assigned negative parity by the authors of Ref. [33] based on single particle Weisskopf estimates and the observed level scheme.

A measurement of $1.0(^{+0.8}_{-0.2})$ ps was placed here on the 6141(2) keV state, the central value being consistent with the limits of 1 ps $< \tau <$ 250 ps placed in Ref. [33]. The higher sensitivity to this transition in this work compared to Ref. [33] is likely due to the implementation of a lead stopper (compared to gold); however, statistics in the 4667(2)-keV transition depopulating the 6141(2) keV state are limited. The 4667(2)-keV transition is the highest-energy transition observed in this work originating from ^{28}Mg.

The lifetime of the 6530.3(14) keV, $(4,5)^-$ state was found to be $3.9(^{+0.8}_{-0.7})_{\mathrm{stat.}}(5)_{\mathrm{stop.}}(2)_{\mathrm{targ.}} \times 10^2$ fs, longer than the previous measurement of $1.9(6) \times 10^2$ fs made in Ref. [33]. However, the longer measurement presented here may be partially explained through the difference in stopping powers of the backing materials used.

The observation of these two states, and subsequent measurements demonstrating that they are indeed long lived, indicates that further precision measurements of these two states may be instrumental in understanding shell evolution. Indeed, the long-lived nature and negative parity of these states points towards intruder configurations, and in neighboring nuclei analogous states are isomeric (e.g., Refs. [11,20,60]).

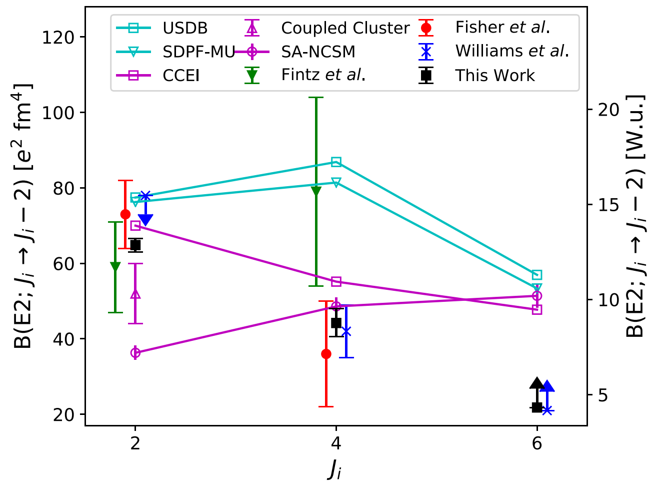

FIG. 8. $B(E2)$ values as a function of initial state spin for the yrast band in ^{28}Mg. Results shown for experimental data from this work alongside previous results from Refs. [33,36,38] and theoretical calculations.

B. Collectivity in the yrast band

Within the yrast band of ^{28}Mg, $B(E2)$ values are seen to decrease with increasing spin. Figure 8 shows $B(E2)$ values for each of the three transitions observed in the yrast band of ^{28}Mg, alongside those measured in Refs. [33,36,38]. The limit on the $B(E2; (6_1^+) \rightarrow 4_1^+)$ transition is such that no conclusions can be made either on the absolute transition strength or its relation to either of the other two yrast transitions.

For comparison, calculations from two phenomenological models are shown: the USDB [61] and SDPF-MU [62] interactions with effective charges of $e_p = 1.5e$ and $e_n = 0.5e$. For SDPF-MU calculations, protons were restricted to the sd shell while one-neutron excitations were permitted to the pf shell.

Calculations were also performed using the coupled-cluster effective interaction (CCEI) [63], a many-body method employing a chiral potential. CCEI calculations used 13 major harmonic oscillator shells with $\hbar\omega = 20$ MeV. Cutoff energies of $\Lambda_{NN} = 500$ MeV and $\Lambda_{3N} = 400$ MeV were used for the chiral next-to-next-to-next-to-leading order nucleon-nucleon (N3LO NN) and N2LO $3N$ interactions respectively, and effective charges used were also $e_p = 1.5e$ and $e_n = 0.5e$.

Additionally, *ab initio* coupled-cluster calculations starting from a prolately deformed Hartree-Fock reference state and the chiral NN and $3N$ interaction 1.8/2.0 (EM) [64] were performed. The calculations used nine major haronic oscillator shells and frequencies $\hbar\omega = 10, 12, 14, 16, 18$ MeV. The low-lying collective excitations and the reduced electromagnetic quadrupole transition probability $B(E2; 2_1^+ \rightarrow 0^+_{\mathrm{g.s.}})$ were computed with the angular momentum projection after variation employing coupled-cluster methods developed in Refs. [65–67]. Uncertainties resulting from the applied methods and finite model space were estimated following the procedures of Ref. [67]. It is important to note here that the coupled-cluster calculations are performed without the use of effective charges.

Finally, the *ab initio* symmetry-adapted no-core shell model (SA-NCSM) [68,69] was also used with the NNLO$_{\text{opt}}$ chiral potential [70] with $\hbar\omega = 15$ MeV and no effective charges. Lower and upper limits correspond to calculations with 9 and 11 major harmonic oscillator shells respectively, thus, the reported uncertainties exclude effects from oscillator frequency or the interactions due to current limitation in computational resources.

Before the measurements presented in this work, experimental data were insufficiently precise to permit distinction between various theoretical models. The present data show a $B(E2;\, 2_1^+ \to 0_{\text{g.s.}}^+)$ greater than the $B(E2;\, 4_1^+ \to 2_1^+)$, a result captured by CCEI calculations, but not by valence space shell models or the SA-NCSM. Using the standard effective charges [63], calculated strengths using CCEI are systematically overpredicted. Experimental $B(E2)$ strengths are well reproduced for the $4_1^+ \to 2_1^+$ and $2_1^+ \to 0_{\text{g.s.}}^+$ transitions using effective charges of $e_p = 1.45e$ and $e_n = 0.45e$, slightly lower than the nominal effective charges, indicating that valence nucleons likely play a greater role in the yrast transitions compared to the core nucleons [71]. However, while there is no *a priori* reason to reduce the effective charges, this is seen in other work on *sd*-shell nuclei, for example in the USDB calculations shown in Ref. [23] studying ^{32}Si, another nucleus bordering the island of inversion, and in Ref. [72] when studying the *sd* shell systematically. The coupled-cluster calculations performed without the use of effective charges produce a $B(E2;\, 2_1^+ \to 0_{\text{g.s.}}^+)$ slightly smaller than the measured value.

The overall suppression of collectivity observed in ^{28}Mg is captured by SA-NCSM calculations, agreeing with the $B(E2;\, 4_1^+ \to 2_1^+)$ measurement but underpredict the $B(E2;\, 2_1^+ \to 0_{\text{g.s.}}^+)$. This reduction in collectivity can be explained as a result of competing shapes (e.g., Ref. [73]), and as shown in Ref. [33], the SA-NCSM calculations show a clear deviation from a rigid-rotor picture and towards strong shape-mixing.

C. Collectivity across the Mg isotopic chain

To study neutron shell evolution and the onset of the island of inversion, transition strengths were examined where data exist for both the $4_1^+ \to 2_1^+$ and $2_1^+ \to 0_{\text{g.s.}}^+$ transitions across the Mg isotopic chain.

1. *B(E2; $4_1^+ \to 2_1^+$)*

Only four transition strengths are reported in Ref. [55] for $4_1^+ \to 2_1^+$ transitions in even-even Mg nuclei, with the highest-N nucleus being ^{28}Mg. These evaluated transtion strenghts are plotted alongside the measurement from this work in Fig. 9. No notable trend or pattern is observed from these strengths, though nuclei with $N \geqslant 18$ have no recorded measurements. Additional measurements of these nuclei, or an increase in precision for the transition strengths in ^{22}Mg and ^{24}Mg, may allow further studies to proceed and conclusions to be drawn.

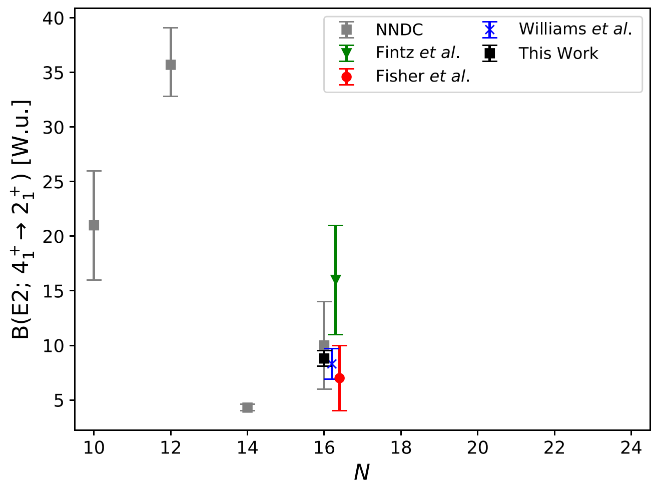

FIG. 9. $B(E2;\, 4_1^+ \to 2_1^+)$ transition strengths across the Mg isotopic chain. Data from this work (black) plotted with evaluated results from Ref. [55] and previous work from Refs. [33,36,38].

2. *B(E2; $2_1^+ \to 0_{\text{g.s.}}^+$)*

With the precision measurement of the $B(E2;\, 2_1^+ \to 0_{\text{g.s.}}^+)$ transition strength presented in this work, the evolution across the Mg isotopic chain becomes much clearer (Fig. 10). Using the existing adopted values for transition strengths from the NNDC [55], the trend is such that there is a sharp decrease leaving stability, followed by relative constancy in the midupper *sd* shell, and an increase on reaching $N = 20$, the island of inversion, and the influence of *pf*-shell configurations. The lone exception to the observed trend is ^{30}Mg, shown to have a reduced transition strength compared to neighboring Mg nuclei.

It is important to note that the NNDC-adopted value [55] for ^{28}Mg is the result of the two measurements presented in Refs. [36] and [38], and that individually these measurement could lead to different possible conclusions.

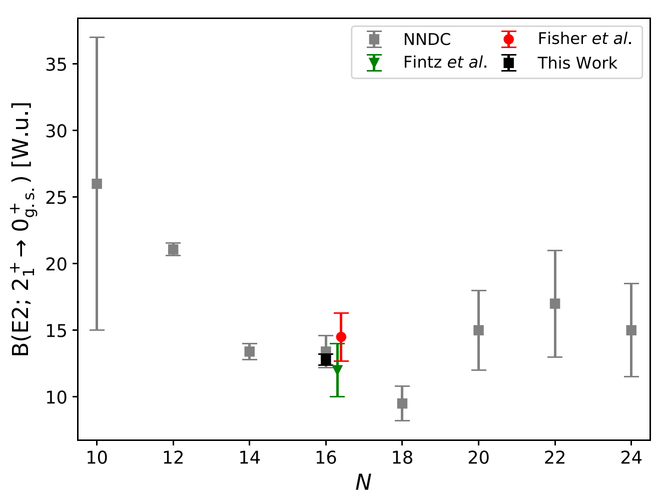

FIG. 10. $B(E2;\, 2_1^+ \to 0_{\text{g.s.}}^+)$ transition strengths across the Mg isotopic chain. Data from this work (black) plotted with evaluated results from Ref. [55] and previous work from Refs. [36,38].

Though the precision of the measurements are insufficient for firm statements, when taken alone, Fintz *et al.*'s [36] measurement would indicate a smooth and continual decrease in the transition strength from stability at $N = 12$ (^{24}Mg) all the way to $N = 18$ (^{30}Mg), while Fisher *et al.*'s [38] measurement would suggest that the transition strength in ^{30}Mg is anomously low. With the new measurement presented here, it becomes clear that the measured transition strength in ^{30}Mg seems anomously low in the context of the Mg isotopic chain, and that this may be of particular importance for understanding the onset of the $N = 20$ island of inversion.

VI. CONCLUSIONS

In conclusion, we present the measurement of excited state lifetimes in ^{28}Mg using both DSAM and RDM techniques to provide sensitivity to both short- and long-lived states. The results demonstrate the importance of studying ^{28}Mg to understand the contribution of intruder, pf-shell orbitals in the structure of sd-shell nuclei, multiple nucleons away from the $N = 20$ island of inversion. The increased precision of the $B(E2)$ measurements of the $4_1^+ \rightarrow 2_1^+$ and $2_1^+ \rightarrow 0_{\text{g.s.}}^+$ transitions in the yrast band of ^{28}Mg demonstrate a clear loss of collectivity within ^{28}Mg itself, and the $B(E2; 2_1^+ \rightarrow 0_{\text{g.s.}}^+)$ measurement highlights the evolution of yrast structure across the Mg isotopic chain. Combined with the measurement made here, a future precision measurement of the $B(E2; 2_1^+ \rightarrow 0_{\text{g.s.}}^+)$ in ^{30}Mg would further constrain this evolution and provide significant guidance for theoretical models.

In total, these results enable tighter constraints to be placed on chiral potentials which drive the degree of shape-mixing in nuclei and include noncentral tensor contributions to the nuclear interaction, essential for understanding how the $N = 20$ island of inversion forms. Precision transition rate measurements, such as those presented here, are thus crucial for further developments of QCD-inspired models of effective nuclear interactions.

ACKNOWLEDGMENTS

The authors appreciate the support of the ISAC Operations Group at TRIUMF and the Simon Fraser University Electronics and Machine Shops. This work was supported by the NSERC Discovery grant program. TRIUMF receives federal funding through a contribution agreement with the National Research Council of Canada. This work was also supported by the U.S. Department of Energy under Contract No. DE-FG02-93ER40789, the U.S Department of Energy, Office of Science, Office of Nuclear Physics, under Award No. DE-SC0023532, under the FRIB Theory Alliance Award No. DE-SC0013617, under SciDAC-5 (NUCLEI collaboration) Grant No. DE-FG02-97ER41014, and by the Quantum Science Center, a National Quantum Information Science Research Center of the U.S. Department of Energy. Computer time was provided by the Innovative and Novel Computational Impact on Theory and Experiment (INCITE) programme. This research used resources from the Oak Ridge Leadership Computing Facility located at Oak Ridge National Laboratory, which is supported by the Office of Science of the U.S. Department of Energy under Contract No. DE-AC05-00OR22725. P.C.S. acknowledges financial support from SERB (India), No. CRG/2022/005167.

[1] C. Thibault *et al.*, Phys. Rev. C **12**, 644 (1975).
[2] E. K. Warburton, J. A. Becker, and B. A. Brown, Phys. Rev. C **41**, 1147 (1990).
[3] Y. Utsuno, T. Otsuka, T. Mizusaki, and M. Honma, Phys. Rev. C **60**, 054315 (1999).
[4] T. Otsuka, T. Suzuki, R. Fujimoto, H. Grawe, and Y. Akaishi, Phys. Rev. Lett. **95**, 232502 (2005).
[5] C. R. Hoffman *et al.*, Phys. Rev. Lett. **100**, 152502 (2008).
[6] R. Kanungo *et al.*, Phys. Rev. Lett. **102**, 152501 (2009).
[7] H. L. Crawford *et al.*, Phys. Rev. C **93**, 031303(R) (2016).
[8] N. Kitamura *et al.*, Phys. Rev. C **105**, 034318 (2022).
[9] G. Neyens, Phys. Rev. C **84**, 064310 (2011).
[10] W. Schwerdtfeger, P. G. Thirolf, K. Wimmer, D. Habs, H. Mach, T. R. Rodriguez, V. Bildstein, J. L. Egido, L. M. Fraile, R. Gernhäuser, R. Hertenberger, K. Heyde, P. Hoff, H. Hübel, U. Köster, T. Kröll, R. Krücken, R. Lutter, T. Morgan, and P. Ring, Phys. Rev. Lett. **103**, 012501 (2009).
[11] F. Rotaru *et al.*, Phys. Rev. Lett. **109**, 092503 (2012).
[12] B. A. Brown and B. H. Wildenthal, Annu. Rev. Nucl. Part. Sci. **38**, 29 (1988).
[13] B. A. Brown, Physics **3**, 104 (2010).
[14] A. O. Macchiavelli *et al.*, Phys. Rev. C **94**, 051303(R) (2016).
[15] L. Fortunato, J. Casal, W. Horiuchi, J. Singh, and A. Vitturi, Commun. Phys. **3**, 132 (2020).
[16] A. Revel *et al.*, Phys. Rev. Lett. **124**, 152502 (2020).
[17] D. G. McNeel *et al.*, Phys. Rev. C **103**, 064320 (2021).
[18] P. T. MacGregor *et al.*, Phys. Rev. C **104**, L051301 (2021).
[19] M. Holl *et al.*, Phys. Rev. C **105**, 034301 (2022).
[20] J. Williams *et al.*, Phys. Rev. C **108**, L051305 (2023).
[21] R. S. Lubna *et al.*, Phys. Rev. C **108**, 014329 (2023).
[22] R. S. Lubna *et al.*, Phys. Rev. C **109**, 014309 (2024).
[23] J. Heery *et al.*, Phys. Rev. C **109**, 014327 (2024).
[24] T. Otsuka, A. Gade, O. Sorlin, T. Suzuki, and Y. Utsuno, Rev. Mod. Phys. **92**, 015002 (2020).
[25] P. E. Garrett, M. Zielińska, and E. Clément, Prog. Part. Nucl. Phys. **124**, 103931 (2022).
[26] A. Bohr and B. R. Mottelson, *Nuclear Structure, Volume 2: Nuclear Deformations* (W. A. Benjamin, Reading, MA, 1975).
[27] O. S. Kirsebom *et al.*, Phys. Rev. C **93**, 025802 (2016).
[28] M. R. Dunlop *et al.*, Phys. Rev. C **96**, 045502 (2017).
[29] B. Fernández-Domínguez *et al.*, Phys. Lett. B **779**, 124 (2018).
[30] J. S. Randhawa *et al.*, Phys. Rev. C **99**, 021301(R) (2019).
[31] P. Ruotsalainen *et al.*, Phys. Rev. C **99**, 051301(R) (2019).
[32] A. Matta *et al.*, Phys. Rev. C **99**, 044320 (2019).
[33] J. Williams *et al.*, Phys. Rev. C **100**, 014322 (2019).
[34] N. Kitamura *et al.*, Phys. Rev. C **102**, 054318 (2020).
[35] H. Nishibata *et al.*, Phys. Rev. C **102**, 054327 (2020).
[36] P. Fintz *et al.*, Nucl. Phys. A **197**, 423 (1972).
[37] B. Rastegar, G. Guillaume, P. Fintz, and A. Gallmann, Nucl. Phys. A **225**, 80 (1974).

[38] T. R. Fisher *et al.*, Phys. Rev. C **7**, 1878 (1973).
[39] J. Dilling, R. Krücken, G. Ball, R. Krücken, and G. Ball, Hyperfine Interact. **225**, 1 (2014).
[40] G. Hackman and C. E. Svensson, Hyperfine Interact. **225**, 241 (2014).
[41] J. Williams *et al.*, Nucl. Instrum. Methods A **939**, 1 (2019).
[42] P. Voss *et al.*, Nucl. Instrum. Methods A **746**, 87 (2014).
[43] A. Dewald, O. Möller, P. Petkov, O. Möller, and P. Petkov, Prog. Part. Nucl. Phys. **67**, 786 (2012).
[44] Micromatter Technologies Inc. (May 2021), www.micromatter.com.
[45] A. Chester *et al.*, Phys. Rev. C **96**, 011302(R) (2017).
[46] A. Chester *et al.*, Nucl. Instrum. Methods A **882**, 69 (2018).
[47] K. W. Allen, *The Electromagnetic Interaction in Nuclear Spectroscopy* (North Holland, Amsterdam, 1975), pp. 311–339.
[48] J. P. Greene, P. J. Voss, and K. Starosta, J. Radioanal. Nucl. Chem. **299**, 1121 (2014).
[49] A. B. Garnsworthy *et al.*, Nucl. Instrum. Methods A **853**, 85 (2017).
[50] S. Hinds, H. Marchant, and R. Middleton, Proc. Phys. Soc. **78**, 473 (1961).
[51] K. Starosta *et al.*, Phys. Rev. Lett. **99**, 042503 (2007).
[52] S. Baker and R. D. Cousins, Nucl. Instrum. Methods Phys. Res. **221**, 437 (1984).
[53] J. Williams *et al.*, Nucl. Instrum. Methods A **859**, 8 (2017).
[54] V. Weisskopf, Phys. Rev. **52**, 295 (1937).
[55] National Nuclear Data Center (NNDC) (Database Version 3.0), nndc.bnl.gov/nudat3/.
[56] C. Patrignani, Chin. Phys. C **40**, 100001 (2016).
[57] ICRU Report, J. ICRU **5**, 1 (2005).
[58] J. F. Ziegler, M. D. Ziegler, and J. P. Biersack, Nucl. Instrum. Methods B **268**, 1818 (2010).
[59] J. Williams *et al.*, Phys. Rev. C **102**, 064302 (2020).
[60] T. J. Gray *et al.*, Phys. Rev. Lett. **130**, 242501 (2023).
[61] B. A. Brown and W. A. Richter, Phys. Rev. C **74**, 034315 (2006).
[62] Y. Utsuno, T. Otsuka, B. A. Brown, M. Honma, T. Mizusaki, and N. Shimizu, Phys. Rev. C **86**, 051301(R) (2012).
[63] G. R. Jansen, M. D. Schuster, A. Signoracci, G. Hagen, and P. Navratil, Phys. Rev. C **94**, 011301(R) (2016).
[64] K. Hebeler, S. K. Bogner, R. J. Furnstahl, A. Nogga, and A. Schwenk, Phys. Rev. C **83**, 031301(R) (2011).
[65] Y. Qui, T. M. Henderson, J. Zhao, and G. E. Scuseria, J. Chem. Phys. **147**, 064111 (2017).
[66] G. Hagen, S. J. Novario, Z. H. Sun, T. Papenbrock, G. R. Jansen, J. G. Lietz, T. Duguet, and A. Tichai, Phys. Rev. C **105**, 064311 (2022).
[67] Z. H. Sun *et al.*, arXiv:2404.00058.
[68] T. Dytrych, K. D. Launey, J. P. Draayer, D. J. Rowe, J. L. Wood, G. Rosensteel, C. Bahri, D. Langr, and R. B. Baker, Phys. Rev. Lett. **124**, 042501 (2020).
[69] K. D. Launey, A. Mercenne, and T. Dytrych, Annu. Rev. Nucl. Part. Sci. **71**, 253 (2021).
[70] A. Ekström *et al.*, Phys. Rev. Lett. **110**, 192502 (2013).
[71] A. Bohr and B. R. Mottelson, *Nuclear Structure, Volume 1: Single Particle Motion* (W. A. Benjamin, Amsterdam, 1969).
[72] S. R. Stroberg, J. Henderson, G. Hackman, P. Ruotsalainen, G. Hagen, and J. D. Holt, Phys. Rev. C **105**, 034333 (2022).
[73] N. D. Heller, G. H. Sargsyan, K. D. Launey, C. W. Johnson, T. Dytrych, and J. P. Draayer, Phys. Rev. C **108**, 024304 (2023).